Magnetic-resonance-imaging–coupled broadband near-infrared tomography system for small animal brain studies

Heng Xu, Roger Springett, Hamid Dehghani, Brian W. Pogue, Keith D. Paulsen, and Jeff F. Dunn

A novel magnetic-resonance-coupled broadband near-infrared (NIR) tomography system for small animal brain studies is described. Several features of the image formation approach are new in NIR tomography and represent major advances in the path to recovering high-resolution hemoglobin and oxygen saturation images of tissue. The NIR data were broadband and continuous wave and were used along with a second-derivative-based estimation of the path length from water absorption. The path length estimation from water was then used along with the attenuation spectrum to recover absorption and reduced scattering coefficient images at multiple wavelengths and then to recover images of total hemoglobin and oxygen saturation. Going beyond these basics of NIR tomography, software has been developed to allow inclusion of structures derived from MR imaging (MRI) for the external and internal tissue boundaries, thereby improving the accuracy and spatial resolution of the properties in each tissue type. The system has been validated in both tissue-simulating phantoms, with 10% accuracy observed, and in a rat cranium imaging experiment. The latter experiment used variation in inspired oxygen (FiO_2) to vary the observed hemoglobin and oxygen saturation images. Quantitative agreement was observed between the changes in deoxyhemoglobin values derived from NIR and the changes predicted with blood-oxygen-level-dependent (BOLD) MRI. This system represents the initial stage in what will likely be a larger role for NIR tomography, coupled to MRI, and illustrates that the technological challenges of using continuous-wave broadband data and inclusion of *a priori* structural information can be met with careful phantom studies.   © 2005 Optical Society of America

    OCIS codes: 110.6970, 300.6340, 120.3890.

1. Introduction

In tissue, near-infrared (NIR) wavelengths of 700–900 nm are absorbed mostly by the chromophores oxy-hemoglobin (HbO_2), deoxyhemoglobin (HbR), and water. In some clinical and experimental situations it would be useful to quantify these compounds in order to indicate metabolic activities, functional changes, or presence and staging of disease.[1–3]

H. Xu (heng.xu@dartmouth.edu), H. Dehghani (hamid.dehghani@dartmouth.edu), B. W. Pogue, and K. D. Paulsen are with the Thayer School of Engineering, 8000 Cummings Hall, Dartmouth College, Hanover, New Hampshire 03755. R. Springett (roger.springett@dartmouth.edu) and J. Dunn (jeff.dunn@dartmouth.edu) are with the Department of Radiology, Dartmouth Medical School, Hanover, New Hampshire 03755. J. Dunn is also with the University of Calgary, Calgary Alberta T2N 4N1, Canada.

The fact that NIR is nonionizing raises its value for *in vivo* studies, where minimal interference is desired. To date, many NIR spectroscopy-based studies of hemoglobin changes in biological tissues have been completed. These spectroscopic methods involve a minimum of two wavelengths—those corresponding to ones above and those below the isobathic wavelength of deoxyhemoglobin and oxyhemoglobin, near 800 nm,[4,5] although it is generally believed that more accuracy can be achieved with additional numbers of wavelengths to improve the spectroscopic information.[6–8] The ultimate extension of this is to take a broadband approach, where light of a broad spectral width is transmitted into the tissue and a spectrum is detected by use of the combination of a spectrograph and a CCD camera.[9,10] With multispectral data, other chromophores, such as water, lipid, and cytochrome, can be analyzed together with hemoglobin, and, moreover, the microscopic scattering particle size, density, and distribution can be studied from the scattering coefficient spectrum.[8,11] All of

these investigations appear to support the hypothesis that more spectral bandwidth leads to a better characterization of tissue.

In addition to the spectral bandwidth effect, NIR investigations would be greatly improved if the spectral information could be enhanced by improved spatial resolution. Such spatial information is difficult to reconstruct, since light scatters as it passes through biological samples—causing the paths of travel to be blurred significantly and limiting the resolution to that defined by the scattering coefficient of the tissue.[12] Current advances in optical image reconstruction and in the prediction of optical scattering are now making it possible to develop a true imaging system in which absorption and scattering properties can be obtained in either two- or three-dimensional space with modest spatial resolution.[13,14] Diffuse optical tomography systems in which multiple source and detection fibers are spaced over the tissue surface are built to collect the boundary data for reconstruction of internal optical properties. This is especially important for brain and breast studies in which the region of interest (tumor) often occurs in the deep tissue.[15,16] Most of these systems are either time-domain systems, in which the time-resolved tissue response to a pulsed laser is recorded, or frequency-domain systems, in which the frequency-dependent signal from a modulated laser source is detected after passing through the tissue. Our recent studies[17,18] show that absorption and scattering images also can be reconstructed with steady-state measurements (i.e., the light is a continuous wave) by applying assumptions about the path length that is due to water at specific wavelength bands, together with the second-differential analysis of the broadband spectrum to estimate the optical path length. This type of broadband system not only has the advantage of simplicity in design and implementation but also has the potential to allow better characterization.

Diffuse optical imaging will always suffer from comparatively low spatial resolution and accordingly sacrificed sensitivity regardless of the geometry and number of measurements. The nature of the diffuse propagation of the signal leads to an ill-posed problem in solving the inverse algorithm to recover an image. However, significant improvement is possible when *a priori* information is included in the image reconstruction.[19] Previous researchers showed that this can be done by incorporating the high-resolution structure images provided by other modalities, such as magnetic resonance imaging[20,21] (MRI), ultrasound,[22] and x-ray.[23] We also have investigated the use of a dual-modality MRI–NIR system, whereby the structural information from the MRI can be used to provide *a priori* constraints to reconstruction of functional images available from the NIR data.[24,25] We are interested in the imaging of the small animal brain to study cerebral oxygenation within infarcts and tumors or within hypoxic–ischemic sensitive regions of the brain such as the hippocampus. These studies are aimed at providing the best resolution and contrast available by combining the benefits of
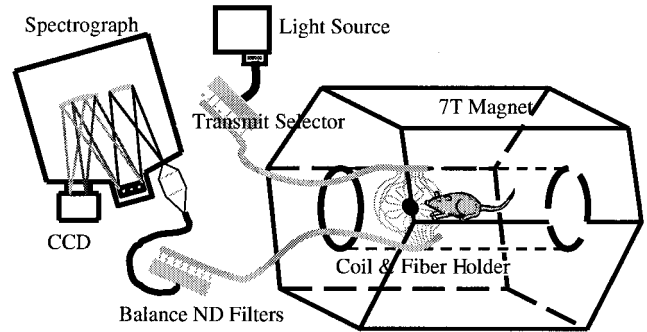

Fig. 1. Schematic design of the MRI-coupled broadband NIR tomography system, for conceptual illustration. It has 8 source and 8 detector fibers alternately surrounding the tissue in the magnet, yielding 64 attenuation spectra from 700–900 nm.

both MRI and the NIR system to permit the better understanding of physiology and pathophysiology, taking the best features of both systems to create a better functional imaging tool.

This paper details the design and operation of a MRI-coupled broadband NIR tomography system in Section 2. Each of eight source optodes transmits broadband NIR light (700–900 nm) in an alternating pattern, and attenuated spectra from the tissue are simultaneously obtained from each of eight detector optodes. The fiber-optic interface and MRI coil are coupled, and images can be acquired simultaneously with NIR and MRI. In Section 3 we outline how the second-differential spectral analysis is applied and how *a priori* information can be incorporated into the image reconstruction. In Section 4 phantom studies and an *in vivo* animal trial are presented.

2. Instrumentation

The intended function of the instrumentation is to measure the complete attenuation spectrum over the wavelength range 700–900 nm from eight transmitting fibers and eight receiving fibers placed alternately around the rat head in a MRI magnet. The system uses parallel detection so that each transmitting fiber is illuminated in sequence, and the attenuation spectra from all eight receiving fibers are collected using a two-dimensional charge-coupled detector (CCD EEV CCD05-30-219, Wright Inc., UK) simultaneously through a spectrograph system (Triax320m, JY Horiba, Edison, New Jersey).

Figure 1 depicts the diagram of our MRI-coupled broadband NIR tomography system. The optical system and the MRI console are coupled at the phantom–animal interface but work independently. This section describes the major components that compose the NIR–MRI system (see Fig. 2): A, light source; B, light delivery; C, fiber-optic interface and MRI coil; D, spectrograph and CCD detector; and finally the data calibration procedure. A panorama of the system on the bench table is presented in Fig. 2 together with enlarged photographs of components B and C.
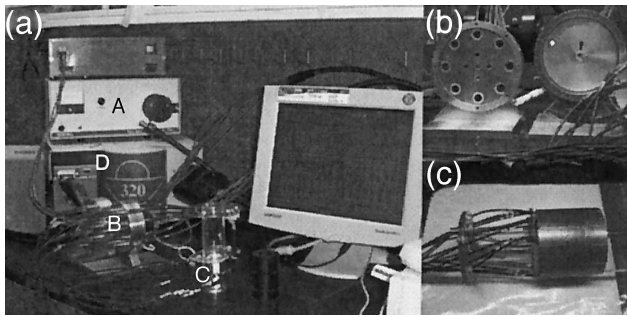
Fig. 2. (a) Photograph of the system is shown with marked components: A, light source; B, light delivery switching stages; C, fiber-optic interface and MRI coil; D, spectrograph and CCD detector. Enlarged photographs of components B and C are shown in (b) and (c), respectively.

A. Light Source

The system uses a fiber-optic illuminator (Model 77501, Oriel Instruments, Inc.) as the light source. It is a self-contained unit, in which a built-in regulated 12-V dc supply powers a 100-W broadband quartz–tungsten halogen lamp, emitting in the region 250–2500 nm. The lamp output is collimated and refocused onto a 11-mm brass ferrule on which eight 1-mm fibers are epoxied and arranged in a 4×2 geometry to match the image of the filament. A 610-nm-long pass filter (Model RG610, Schott NA, Inc., New York) installed within the collimated region of the beam is used to remove redundant visible wavelengths to reduce the local heating of the tissue. The overall system response peaks near 800 nm with 0.3 OD at 700 nm and 0.1 OD at 900 nm.

B. Light Delivery

To select one of the eight source fibers in sequence, they are connected to a shutter wheel. This consists of a rotating disk with an aperture, all enclosed within an aluminum housing. Imaging the rat head requires a system with a high dynamic range, because the attenuation difference between the nearest and farthest neighbors are typically 3 OD. The useful dynamic range of a CCD is typically 2 OD, e.g. between spectra with a maximum signal of 100,000 and 1000 electrons. To increase the dynamic range of the CCD, the preliminary design used a custom readout mode in which the weaker channels were vertically binned over the whole height of the channel (42 pixels) and a single spectrum read out, whereas the strongest channels were vertically binned over two rows and 21 spectra read out and digitally binned. This increases the dynamic range by approximately 1.3 OD. Although the imaging capabilities of the spectrograph were sufficient to completely separate the channels, it was found that imperfections on the surface of the CCD window and retroreflections from the edges of the CCD windows produced a patterned cross talk that was not insignificant between the strongest and weakest channels. For this reason it was decided to balance the input intensity of each channel with neutral-density filters. As the neighbor index of each

receiving fiber changes depending on which transmitting fiber is active, the simplest implementation is to use a rotating wheel similar to the transmitting stage but with neutral-density filters instead of a single aperture. The disadvantage of this system is that the attenuation reduces the signal-to-noise ratio of the attenuation spectrum and is most severe on the nearest-neighbor channels spectra, which have the smallest dynamic range. On this balance wheel four pairs of neutral-density filters (OD = 0, 0.5, 1.0, 2.0; Melles Griot Inc., California) are currently installed. Both the shutter wheel and the balance wheel are driven by a stepper motor (ACS Machine Controls, Massachusetts). The motion and synchronization of both wheels are controlled by the driver broad (SMA32-A, ACS, Massachusetts) under the supervision of the computer. On both sides of the wheel eight SMA collimators are installed to couple the light from the fibers.

Two types of fiber are used in the system. The first is a 1-mm single-core silicon fiber (N.A. 0.3, Thor Labs, Inc.). One end is terminated in a standard SMA connector and the other is epoxied in a brass ferrule. Sixteen such fibers are used in the short-distance delivery within the bench table where the main body of the system sits, i.e., between the light source and the shutter wheel or between the balance wheel and the spectrograph. The other fiber type is a flexible bundle of diameter 1.5 mm sheathed in PVC and 10 m long to reach the MRI magnet from the bench table (Spectraflex, Schott NA, Inc., New York). The bundle is made from 50-μm fibers, is more flexible, and has a smaller bend radius 8mm than a 1-mm single fiber. One end of the bundle is terminated in a SMA connector, and the other terminated in a ferrule (diameter 1/8 in., length 5/8 in. 1 in. = 2.54 cm) made of black acetal and cemented in epoxy resins.

C. Fiber-Optic Interface and Magnetic-Resonance-Imaging Coil

The MRI console made by Varian has an operating frequency of 15–305 MHz. The magnet was made by Magnex and is a 7-T horizontal bore system with a 12-cm clear bore. A homebuilt birdcage rf coil was constructed on a clear right-circular cylindrical plexiglass with wall thinness of 1/8 in. having eight 6-cm legs, a 4-cm inner diameter, and a copper trace ~4 mm wide. The resonant coil frequency was 300 MHz for the Larmor frequency of protons in a magnetic field of 7 T. Sixteen holes normal to the circular wall were drilled in the same plane perpendicular to the bore axis and distributed equally around the coil without cutting the copper traces. Each fiber optode was manually mounted on the coil and guided through holes into gentle contact with the phantom–tissue surface. Each hole was made to match the size of the 1/8-in. optode and to provide a gentle press fit. This design allows each fiber to move independently, and therefore its radial position can vary by several millimeters to fit the irregular surface of the animal head. The fibers were bent 90° to exit the magnet along the bore axis in the space between

the inner coil and the outer 10-cm-diameter copper shield.

D. Spectrograph and CCD Detector

The eight 1-mm fibers exiting the rotating filter wheel were epoxied into a 25-mm brass ferrule in a line at a pitch of 1.5 mm and height of 11.5 mm. This design allowed a separation of 500 μm between the edges of neighboring fibers. The light from the fibers was collimated with a 25-mm-diameter 60-mm focal-length lens antireflection coated for 650–1000 nm. The collimated light was then focused onto the slits of a spectrograph by a second lens with a diameter of 30 mm and a focal length of 62 mm. The two lenses were mounted on a rod system, allowing focusing, while the first lens was housed in a floating mount on the rod system, allowing x and y directional alignment. The combination of the two lenses gave a magnification of 0.92, so that the image of the fibers on the slits was 10.61 mm high, and the image of a single fiber was ~0.92 mm high. The spectrograph was a Triax 320 m (JY Horiba, Edison, New Jersey) with an aperture at $F4.1$, a 0.32-m focal length, motorized input slits, and a motorized triple grating turret, allowing the gratings to be rotated and changed under computer control. For the majority of the studies a 300-g/mm grating blazed at 1000 nm was used, but we also had a 600-g/mm grating blazed at 1000 nm for use where higher throughput was needed with a reduced spectral range.

Multiple spectra from light imaged at various heights in the entrance slit of the spectrograph could be detected simultaneously with a two-dimensional array. The optics permitted close vertical spacing of signals without cross talk. Therefore the spectrograph was fitted with a CCD camera (Wright Instruments, Enfield, UK) containing an EEV CCD05-30-219 MPP CCD cooled to 205 K. The CCD has 1242 pixels in the wavelength axis and 1152 pixels in the slit axis. The pixels are 22.5 μm × 22.5 μm, and the active area is 27.9 mm × 25.8 mm. The CCD was configured in frame transfer mode, but there was no shield over the store section. The CCD was mounted at 5° to the focal plane in the wavelength axis of the spectrograph to optimize resolution in the wavelength and imaging planes. Furthermore, the CCD was mounted so that the center of the slit fell in the center of the image section of the CCD. Although the store section of the CCD was not shielded, the spectrograph had adequate stray light rejection and imaging capabilities to ensure that negligible light fell on the store section during the readout. The image section was 12.96 mm high and was adequate for the image of the fibers on the slit. The majority of the light from each fiber produced an image 42 pixels high (0.92 mm).

E. Calibration

The calibration procedure was essential to reduce the deterministic bias of the measured signal. Two kinds of calibration were applied: (1) system calibration and (2) model calibration. System calibration was to elim-inate the influence of the variation among all the source–detector combinations. Since our data set is a broadband spectrum, it requires two-dimensional calibration, i.e., wavelength axis calibration and intensity calibration for each source–detector pair. Some components such as the light source may change daily in its output spectrum, so the system needs to be calibrated before every use. For the wavelength axis calibration, a neon lamp (Model 6032, Oriel Instruments, Inc.) was used to align the motorized grating stage to the correct wavelength position. For the intensity calibration, all 64 source–detector pairs were calibrated simultaneously with a white Teflon cylinder phantom. The procedure was to take a measurement on this phantom as intensity reference. The measurement for the target objects was the difference to the reference data set plus the known attenuation of the Teflon phantom as shown in Eq. (1):

$$A_{\mathrm{obj}} = -\ln(I_{\mathrm{obj}}/I_{\mathrm{ref}}) + A_{\mathrm{ref}}, \tag{1}$$

where A_{obj} is the desired system-independent attenuation spectrum of the target, A_{ref} is the premeasured attenuation spectrum on the stable reference phantom, and I_{obj} and I_{ref} are the intensity measurement of the target and the reference, respectively.

Model calibration is a necessary step for image reconstruction to minimize the imperfection in the mathematical model, such as boundary conditions, discretized error, and dimensional difference.[26] The measurement in reality was slightly different from the data simulated by the model and could become a systematic noise to image reconstruction. The differences between data measured from a homogeneous phantom and data calculated from the model are stored and subtracted from measurements of the target object, while homogeneous bulk fitting of data provides the initial guess for image reconstruction.

3. Methods

A. Second-Differential Spectral Analysis

Second-differential spectral analysis is a novel approach to diffuse optical tomography using broadband spectroscopy data.[17,18] It not only provides a strategy to linearly separate chromophore concentrations and scattering coefficients from the attenuation spectrum but also provides a means to estimate the optical path lengths near the water features in the second-differential spectrum (740 and 840 nm). This calculated path length is a secondary measurement independent of the intensity measurement for solving the diffusion approximation equation for both absorption and scattering properties by using amplitude and phase data types. Although several approximations have to be made during the analysis, they are reasonable assumptions based on the physics of light propagation in tissue and the makeup of the chromophores present in tissue.

The attenuation is determined by the optical properties of absorption and reduced scatter $[\mu_a(\lambda), \mu_s{}'(\lambda)]$,
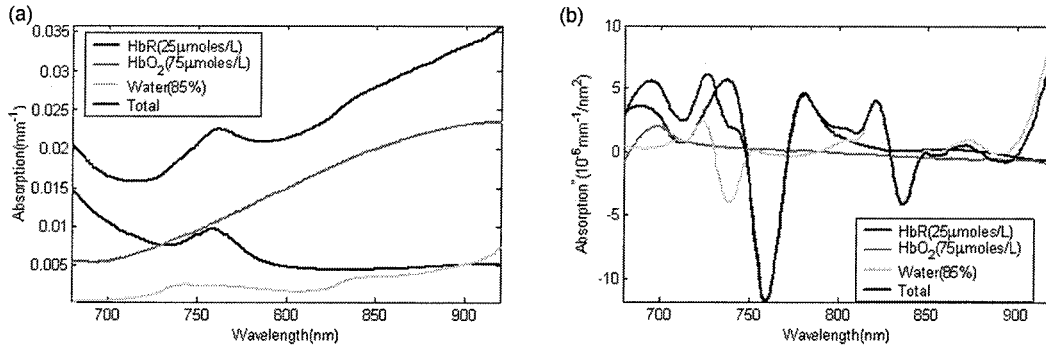
Fig. 3. (a) Examples of typical absorption spectrum and the contributions from individual chromophores are plotted.[27,28] (b) Example of the second-derivative spectrum of absorption as well as the contributions from the corresponding chromophores.

where both coefficients are wavelength dependent; thus the attenuation $A(\lambda)$ is also wavelength dependent. With the chromophores present in the tissue and the weak wavelength dependence of the scattering coefficient of tissue, the second derivative of the attenuation A'' can be expressed by Eq. (2):

$$A'' = \frac{d^2 A}{d\lambda^2} = \rho(\lambda) \frac{d^2 \mu_a}{d\lambda^2}$$

$$= \rho(\lambda) \sum_{i=1}^{M} C_i \frac{d^2 \varepsilon_i}{d\lambda^2} + o_1 = \rho(\lambda) \sum_{i=1}^{M} C_i \varepsilon_i'' + o_1, \quad (2)$$

where ρ is the optical path length, C_i and $d^2 \varepsilon_i / d\lambda^2$ are the concentration and the second derivative (ε_i'') of the extinction coefficient (absorptivity) of the ith chromophore, and o_1 stands for the ignored small terms. The absorption coefficient is the linear combination of the absorption due to individual chromophores as shown in Fig. 3(a). At every wavelength the contribution comes from each chromophore. However, contributions of individual chromophores become sharper and more distinguishable on the wavelength axis in the second-derivative spectrum as shown in Fig. 3(b). Savitzky–Golay filtering was used to calculate the second derivative from the noisy spectral data. This method can be thought of as a generalized moving average when an unweighted linear least-squares fit is performed with a polynomial of a given degree, and second-derivative coefficient can be easily derived from the fitted polynomial coefficients. In our implementation a quartic polynomial with 40-nm span was used to remove high-frequency noise without sacrificing the low-order spectral features.

Because the optical path length only gradually varies with wavelength, it can be approximated by its mean value in a reduced wavelength range where a sharp chromophore feature exists. Therefore, in such a reduced wavelength range, Eq. (2) can be simplified to

$$A'' = \sum_{i=1}^{M} (\rho C_i) \varepsilon_i'' + o_1 + o_2. \quad (3)$$

Here o_2 is the residue due to this approximation.

Since ε_i'' is known and A'' is the observation at N discretized wavelengths, if the small terms o_1 and o_2 are discarded, the matrix form of Eq. (3) is an over-determined linear problem:

$$\mathbf{A''} = \varepsilon'' \rho \mathbf{C}, \quad (4)$$

where $\mathbf{A''}$ is an $N \times 1$ vector, ε'' is an $N \times M$ matrix, and the unknowns are the scalar ρ and M by one-vector $\mathbf{C}$. The unknowns can be solved by the multiregression fitting algorithm. The optical path length and the chromophore concentration are combined; therefore, to qualify either one of them, the other must be provided. In our studies, the water content was ~85% over the entire rat head[29] and could be measured more accurately by the nuclear magnetic resonance system; therefore the optical path length can be calculated.

Water has two prominent second-differential absorption features near 740 and 840 nm, as is seen in Fig. 4(b). To apply the relation in the Eq. (4) and calculate the optical path length near these wavelengths, we empirically choose two reduced wavelength ranges (700–800 and 800–880 nm) to fit the measured attenuation curve. The spectrum is sampled approximately every 1/3 nm. Three chromophores, oxyhemoglobin, deoxyhemoglobin, and water, are typically included in the fitting. Both the measured attenuation spectrum (A) and the absorptivity spectrum (ε) are processed by a 40-nm-width fourth-order polynomial filter to minimize the high-frequency noise, and the second derivatives are calculated at the same time. Examples of measured attenuation, its raw second-derivative data, and the fitted second-derivative data from Eq. (4), along with the residue of fits in both ranges, are shown in Fig. 4, resulting from a liquid phantom that has 60 μmol/L HbR and 1.0% Intralipid. The residue results from the experimental noise and the ignored terms (o_1, o_2) and is more consistent with random and featureless behavior. The energy of this residue is ~5% of the original signal, which implies that our approach does capture the principle component in the second-differential analysis and that exclusion of those small terms is a reasonable and effective approximation to facilitate the analysis. Furthermore, we have shown
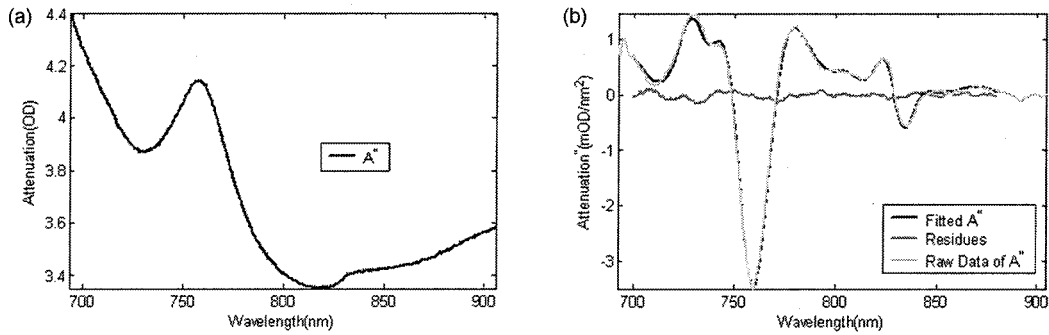
Fig. 4. (a) Measured attenuation spectrum from a homogeneous liquid phantom with 60 µmol/l HbR and 1.0% Intralipid. (b) Raw data of the phantom's second-derivative spectrum are shown, along with the spectrum fitted by SDSA and the residues.

that with those path lengths estimated from the water features, absolute absorption and reduced scattering coefficients can be recovered successfully by using the diffusion approximation to the transport model.[18]

From every attenuation spectrum, path lengths and attenuated light intensities at 740 and 840 nm are calculated, so the overall 8×8 attenuation spectra acquired around the tissue generate two data sets of 64 pairs of path length and intensity measurements with parabolic shape. Each data set is used to reconstruct images of optical properties (μ_a and μ_2') at the corresponding wavelength.

B. Image Reconstruction

The diffusion approximation to the Boltzmann transport equation is an appropriate model to use when light scattering dominates absorption in a medium. In the frequency domain, this approximation is given by

$$- \nabla \cdot D(r) \nabla \Phi(r, \, \omega) + \left(\mu_a + \frac{i\omega}{c}\right)\Phi(r, \, \omega) = q_0(r_0, \, \omega),$$

$$(5)$$

where $q_0(r, \omega)$ is an isotropic light source at position r_0, $\Phi(r, \omega)$ is the photon fluence rate at position r, c is the speed of light in the medium, ω is the frequency of light modulation, and $D = 1/[3(\mu_a + \mu_s')]$ is the diffusion coefficient. The Robin-type (type III) boundary condition is used at interfaces with air or fibers:

$$\Phi(\gamma) + \frac{D}{\alpha} \, \hat{n} \cdot \nabla \Phi(\gamma) = 0,$$

$$(6)$$

where α is a term that incorporates reflection as a result of refractive-index mismatch[30] at the boundary and $\hat{n}$ is the outward normal to the boundary at γ. We use a finite-element method as a general and flexible method for solving the forward problem in arbitrary geometries.[31] That is, for a given μ_a and μ_s' distribution, the finite-element analysis predicts the optical flux at the detection sites for each source excitation. In the inverse problem (image reconstruction) the goal is to estimate the distribution of optical proper-

ties at each mesh node based on the measurement of optical flux at the detector sites on the tissue surface. This is achieved numerically by minimizing the difference between the calculated data ϕ^C and measured data ϕ^M for all source and detector combinations (NM). Typically, this is written as the minimization of χ^2:

$$\chi^2 = \sum_{i=1}^{NM} (\phi_i^C - \phi_i^M)^2.$$

$$(7)$$

Here χ^2 can be minimized in a least-squares sense, that is, setting the derivative equal to zero and using a Newton–Raphson approach to find the set of optical property values which approximate the minimum value. We use a Levenberg–Marquardt algorithm[32] to solve this nonlinear inverse problem by iteratively using the equation

$$a = (J^T J + \lambda I)^{-1} J^T b,$$

$$(8)$$

where $b = (\phi^C - \phi^M)^T$ is the data vector that represents the difference of measured data and calculated data at each iteration and $a = [\delta D; \delta \mu_a]$ is the solution update vector. Here λ is a regularization factor suggested by the Levernberg–Marquardt algorithm to stabilize matrix inversion and $\mathbf{J}$ is the Jacobian matrix for current iteration, which is calculated by the adjoint method. Indeed, the frequency-domain finite-element-method image reconstruction requires measurements of the amplitude and the phase shift of the modulated light, which requires that the calculated optical path length be converted to the phase shift first before the reconstruction.[17] It has been shown in previous studies that at low frequencies the path length is linearly related to the phase shift; thus knowledge of the path length can lead to estimation of the phase shift at lower frequencies. This approach has been outlined in detail in our previous study.[17,25]

Efforts have been made to improve the diffuse image reconstruction by incorporating structural information as a priori,[19,20,24,33] which is typically provided by other modalities such as MRI, x ray, or ultrasound, which has the contrast and the resolution to define the tissue surface and segment tissue types.

Table 1. Summarized Results of Phantom Studies[a]

Phantom	Optical Property	Target Contrast	Without *A Priori*				With *A Priori*			
			Peak	Diff.	Mean	Diff.	Peak	Diff.	Mean	Diff.
A	μ_a	1.03	1.06	+2.9%	1.03	0.0%	1.08	+5.2%	1.04	+1.0%
	μ_s'	1.48	1.45	−2.0%	1.29	−13%	1.50	+1.6%	1.34	−9.8%
B	μ_a	1.44	1.38	−4.2%	1.27	−11%	1.56	+8.4%	1.40	−2.7%
	μ_s'	0.64	0.73	+14%	0.79	+23%	0.66	+3.6%	0.74	+16%
C	μ_a	1.44	1.35	−6.3%	1.25	−13%	1.46	+1.5%	1.37	−4.8%
	μ_s'	1.55	1.62	+4.5%	1.38	−11%	1.59	+2.9%	1.37	−11%

[a]The original optical properties are converted to contrast with the background for convenience. The target values from three types of phantom are listed in the "Target Contrast" column. Reconstructed peak values ("peak") and mean values ("mean") for the inclusion and their differences ("Diff.") from the target are listed for both reconstructions with or without *a priori* information.

To utilize the structural information provided by MRI data, in our case, several techniques have been used. Each of these is discussed in the paragraphs below.

First, the *a priori* information can be used to optimally define the imaging domain. This step is relatively straightforward, since the finite-element method cannot be applied without knowing the tissue volume and the optode positions. The outline of tissue surface can be used to create a finite element mesh in either two or three dimensions, and the tissue type indicated by the MRI segmentation can be assigned as regional information to the mesh. Guided by the impressions caused by fiber–tissue contact, the image plane where the optode ring is and locations of sources and detectors can be determined.

A second level of increasing the *a priori* information is to use it to enhance contrast and resolution in specific regions of interest. Conventional image reconstruction treats the whole image volume with the same priority and a scalar regularization factor λ is used in the Tikhonov regularization scheme [Eq. (6)]. The regularization stabilizes the matrix inversion but sacrifices some contrast and resolution. With *a priori* information of the tissue internal structure, the update of optical properties can be preferentially directed to specific regions of interest. This is accomplished by introducing spatially varying regularization, where regions with known higher average optical properties can be given lower regularization to give them more freedom to update in the interaction process.[20,33,34] By defining the regularization parameter spatially, the optical contrast of region of interest can be improved, yet the high-frequency interior boundaries can be preserved. The performance of this method relies on whether the segmentation provided by MRI represents the true optical contrast and whether the initial properties of reconstruction are close to the true background. The efficacy of this technique was examined by the phantom studies presented in Section 4.

Third, improving the initial values of reconstruction is useful. The initial values, i.e., the initial guess of starting properties, are crucial to recover the true distribution of optical properties.[24,25] The mismatch of the measured data and the calculated data are gradually minimized by iteratively adding the perturbation to the initial guess of optical properties. Previous research has shown that the reconstruction of small heterogeneities can be greatly improved if an initial guess that is close to the true value could be provided. When we studied the functional changes in rat brain during hypoxia, shown in the next section, the structural information was used to achieve the initial baseline image. The functional changes were added to the finite-element-generated data using a calculated baseline homogeneous image for reconstruction.

4. Experiments and Results

A. Phantom Studies

The ability to characterize an embedded scattering or absorbing object was tested in rat head simulating phantoms. The material to build these phantoms is a mixture of ink, TiO$_2$, and gelatin with 85% water. By controlling the amount of ink or TiO$_2$, the absorption or the scattering property could be varied, respectively. These phantoms were cylinders of 27-nm diameter with a 14-nm inclusion near the edge, which has optical properties different from the background, similar to the geometry of a brain within the cranium of a rat. Three types of inclusion are used to build phantoms within the same background: (A) an inclusion with higher scattering; (B) an inclusion with higher absorption and lower scattering; and (C) an inclusion with both properties higher. In Table 1, the "Target Contrast" column gives the optical contrast of the inclusion relative to the background. This contrast was calculated from bulk optical properties of each type of material (either inclusion or background) that were measured with a homogeneous fitting algorithm after a separate homogeneous cylindrical phantom was created with the material. Reconstructed cross-sectional images were generated with a two-dimensional reconstruction program for these phantoms, and these are shown in Figs. 5, 6, and 7, successively. In each figure target images [parts (a)] are shown along with reconstructed images with the conventional method having no *a priori* information [parts (b)] and with reconstructed images with *a priori* information [spatial varying regularization, parts (c)]. Profile cross-section plots of the images are
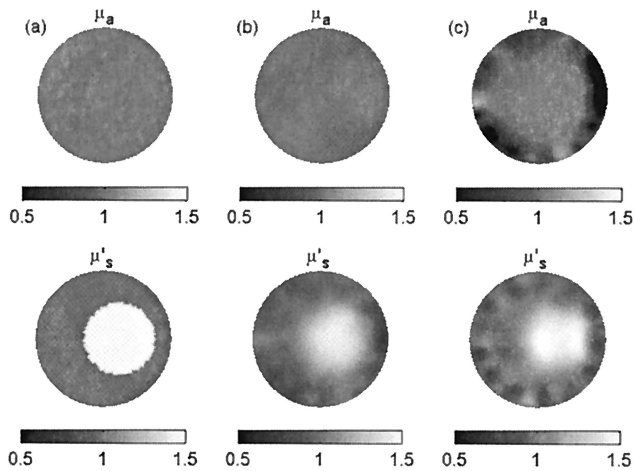
Fig. 5. Absorption and reduced scattering images of phantom A, which has a higher scattering inclusion off the center. (a) Target images, (b) reconstructed images without *a priori* information, (c) reconstructed images with *a priori* information.

Fig. 7. Absorption and reduced scattering images of phantom C, which has a higher absorption and scattering inclusion off the center. (a) Target images, (b) reconstructed images without *a priori* information, (c) reconstructed images with *a priori* information.

shown in Fig. 8 for better visualization of the quantitative values. Reconstructed peak and mean values of the inclusion by the two methods and their difference from the target are listed in Table 1 for comparison. The three-dimensional meshing and image reconstruction are also possible and similar results to the two-dimensional reconstruction were achieved when this was tried, so here the presentation is restricted to the two-dimensional results for simplicity. Optical properties are converted to dimensionless contrasts to the background properties in the table and in all the figures for convenience.

B. *In Vivo* Studies

An example of tomography imaging of *in vivo* of a rat head during hypoxia is shown. An adult male Sprague–Dawley rat was anesthetized (isoflurane

1–1.5%, N_2O 70%, O_2 30%), tracheotomized, mechanically ventilated and fixed in the NIR–MRI coil placed in the magnet. A stack of T_2-weighted 256 × 256 pixel MRI images (voxel dimensions, 137 μm × 137 μm × 1000 μm) was obtained with a 35-mm field of view and repetition (TR) and echo (TE) times of 2000 and 40 ms, respectively. The slice overlapping with the optical fiber ring is shown in Fig. 9(a) and was processed to create a finite-element mesh with regional information for forward problem as shown in Fig. 9(b). A lower-resolution mesh was also generated for the reconstruction basis, as shown in Fig. 9(c). The oxygen fraction in the inspired gas was varied in a sequence of 30%, 15%, 12%, 10%, 100%, 30%, 0%, and 0% with a 10-min interval, while both NIR spectral tomographic data and blood-oxygen-level-dependent MRI data were acquired. The NIR image reconstructed for the initial state was shown in Fig. 9(d). To improve the interpretation of functional changes
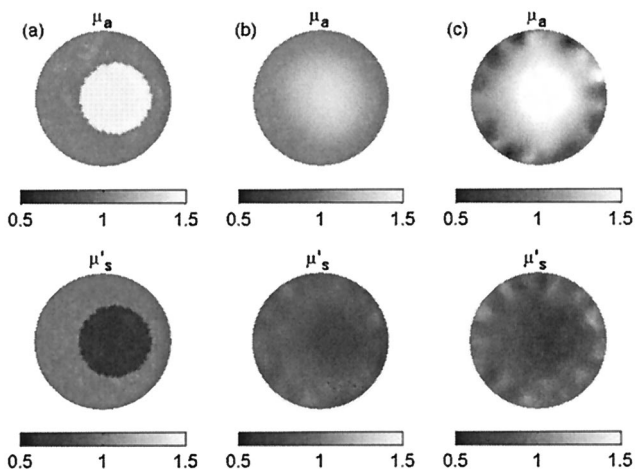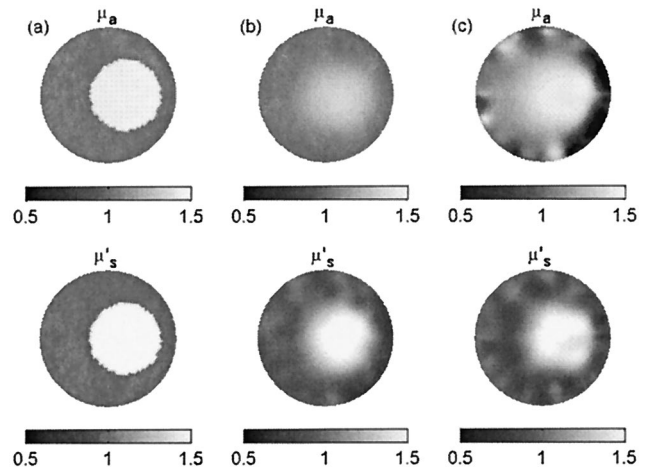

Fig. 6. Absorption and reduced scattering images of phantom B, which has a higher absorption but lower scattering inclusion off the center. (a) Target images, (b) reconstructed images without *a priori* information, (c) reconstructed images with *a priori* information.
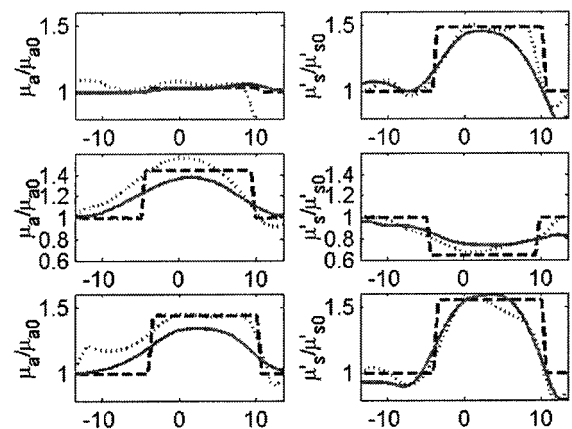

Fig. 8. Horizontal profile transects from the images of Figs. 5, 6, and 7. The contrast distribution for target images (dashed curves) was reconstructed from images without *a priori* information (solid curves) and reconstructed images with *a priori* information (dotted curves).
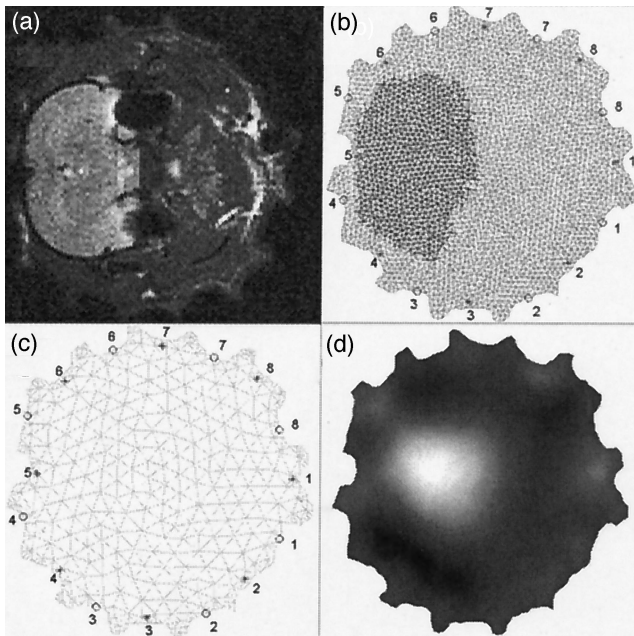
Fig. 9. (a) Anatomically coronal T2-weighted MRI slice of the cranium with impressions caused by fibers all around the periphery. (b) Two-region finite-element fine mesh with labeled source and detector locations, as created from image (a). (c) Coarse mesh as used for reconstruction basis. (d) Reconstructed absorption image in the initial resting state, with the animal breathing a normal 30% oxygen.

Fig. 10. Series of reconstructed absorption images at 740 and 840 nm when different inspired oxygen fractions (FiO$_2$) were given. From left to right, the values correspond to FiO$_2$ of 30%, 15%, 12%, 10%, 100%, 30%, 0%, and death, respectively.

and limit the artifacts, a baseline image of the initial value of latter reconstructions was created with two regions (brain and background), and the initial optical properties of each region were taken from the mean value of the same region in the first reconstructed NIR image. Then the difference in attenuation between the specific measurement times within this hypoxia experiment were calculated and added to the data from the baseline image and were used to recover the functional changes. This procedure provided a data set that matched the model prediction well and yet retained all heterogeneous aspects of the rat imaging. This difference imaging technique is useful in *in vivo* studies, where many factors may degrade the accuracy of modeling. The benefits and limitations of this approach are further discussed below.

A series of reconstructed images at different inspired oxygen level for both 740 and 840 nm are shown in Fig. 10. With the assumption that the absorption changes within the series were due to changes of hemoglobin content and its oxygenation, changes of HbR, HbO$_2$, and HbT can be calculated; the mean values in the brain are shown in Fig. 11(a). The relationship between deoxyhemoglobin concentration and R_2* is shown in Fig. 11(b).

5. Discussion

In Figs. 5, 6, and 7, images reconstructed with *a priori* information clearly provide higher contrast for the inclusion than those reconstructed without it.
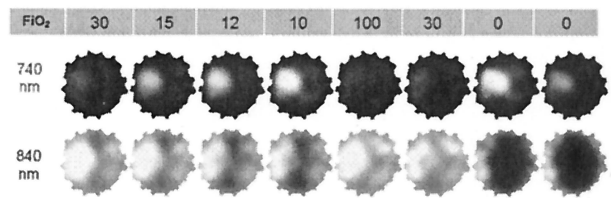
Higher contrast also brings the sharper boundary out, to allow better interpretation of the actual size of the inclusion. This can easily be observed in Fig. 8, where profile plots of the reconstruction with *a priori* information do better approximate the target profiles in the region of the inclusion. Higher background noise is unfortunately observed in those images reconstructed with *a priori* information, and yet these occur mostly near the boundary. The exact cause of these edge artifacts is not fully understood and needs to be explored, yet in previous studies these were clearly demonstrated to be related to model–data mismatch.[35] While improvements to the model can always be made to try to match the data better, earlier studies have clearly indicated that small boundary errors in distance and position can cause large errors in the boundary data, and so it is likely useful to develop calibration strategies in the future that minimize this hypersensitivity to the boundary. Thus the method developed in this paper of using difference data added to a homogeneous fit baseline has been a very successful and workable solution for this particular system.

In Table 1, after reconstruction without *a priori* information, the peak value to the inclusion is within 6% difference from the target on average, and the mean value is within 12% difference from the target. With *a priori* information those differences are improved to 4% and 8%, which means that better quantitative accuracy is achieved.

In the rat image reconstructed from data taken while the rat was in the normal resting state, a region with higher absorption (Fig. 9d) and higher reduced scattering is observed at the position of the brain, agreeing with what was expected. The shape is a little bit different from the true shape of the brain indicated by the MRI, which may be caused by the distortion from artifacts in the image. These artifacts could result from the measurement noise, the heterogeneity of the rat head, positioning error, or a calibration problem on the irregular mesh. These factors are limited by calibrating the latter reconstruction with the baseline image created from this first image. Improved image quality is obtained in those images shown in Fig. 10. Reconstructed optical images clearly showed changes in saturation, indicating that functional changes in the rat can be monitored. The trends of HbR and HbO$_2$ followed predictable trends during hypoxia, but the expected increases of cere-
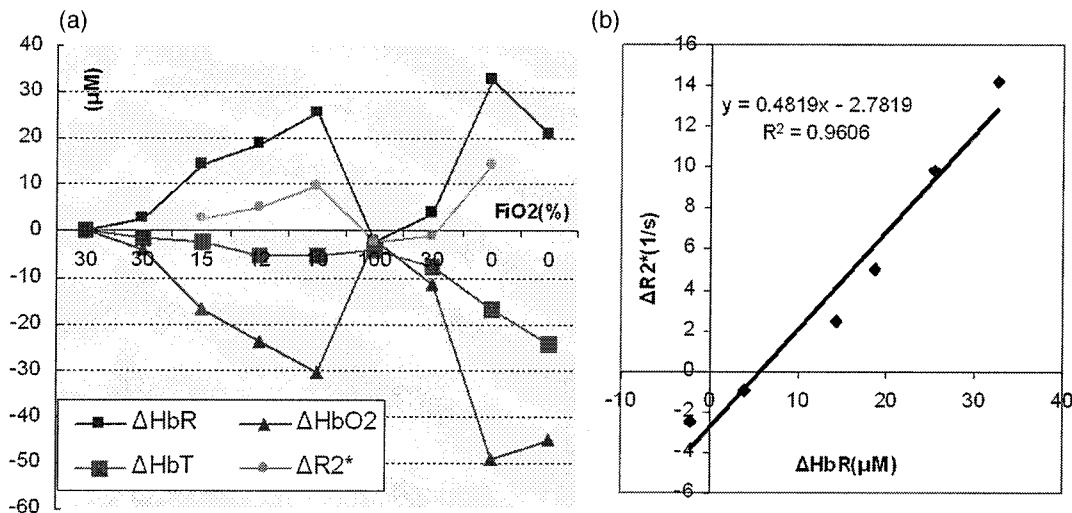
Fig. 11. (a) Changes of HbR, HbO2, HbT (total hemoglobin), and R_2^* are shown with the oxygen fraction. (b) Correlation of HbR and R_2^*.

bral blood volume and HbT were not observed.[36,37] Further experiments are needed to explore this issue. A strong correlation ($r = 0.97$) between deoxyhemoglobin and R_2^* was observed, and the ratio (0.48) was similar to the 0.47 observed by S. Punwani et al.[38] using NIRS without image reconstruction. Such correlations have also been observed in other studies.[39,40] With imaging, the expected value should be higher, since partial volume errors would be reduced. This study is really the first step indicating that both NIR image reconstruction and MRI R_2^* could be quantifiable and directly compared with each other in a manner that would allow spatially resolved comparisons.

Further study is ongoing on how to use the MRI internal structures for constraints and thereby enhance the spatial resolution and potential accuracy of the NIR-derived hemoglobin and oxygen saturation. Since the MRI T1-weighted structures that can be segmented apart are the same ones that would be expected to have different optical properties, it is logical to assume that these could be used as interior *a priori* information. Further analysis of how to optimize the inclusion of *a priori* information is definitely needed and will be completed in a systematic manner with a larger group of animals; however the working principle presented here represents the culmination of several studies in this approach.[17,20,24,41,42] However, implementation of interior spatial structure in a manner that does not constrain the final image too much is nontrivial and requires extensive parameter studies, and so will be the subject of future research.

6. Conclusion

This article describes a novel MRI-coupled broadband NIR tomography system for small animal brain studies. High-resolution tissue images obtained by MRI were applied as *a priori* information in the NIR image reconstruction process. Images of optical properties, absorption, and reduced scattering coefficients can be improved in terms of the quantitative accuracy and the spatial resolution by use of this approach, and therefore this system provides a more straightforward tool to study cerebral physiology and pathophysiology. The NIR system collects 64 broadband attenuation spectra (700–900 nm) from 8 source fibers and 8 detection fibers placed around the animal head in the magnet. Second-differential spectral analysis was applied to high-quality attenuation spectra and estimated optical path lengths for 740 and 840 nm. Absolute absorption and reduced scattering images can be reconstructed on finite-element meshes from the attenuation and path length measurements by use of the diffusion approximation model.

The practice of incorporating MRI structure for external and internal boundary information into NIR image reconstruction has been discussed and demonstrated through phantom studies and an *in vivo* animal study. In the phantom studies various brain-sized inclusions with absorption and scattering contrast different from the background have been reconstructed with relatively high accuracy (~10% difference) even without applying *a priori* information. This verifies that our second-differential spectral analysis does provide a reliable estimate of true optical path length and makes it possible to separate absorption and reduced scattering properties with continuous wave data. Spatially varying the regularization factor and using the structural information have improved reconstructed images both qualitatively and quantitatively, though the improvement is not so significant, since the inclusion has a relatively large size and low contrast. Higher noise near the boundary in the images reconstructed with *a priori* information was observed, which might result from the discontinuity of regularization and will be explored in a future study. Preliminary *in vivo* results on the animal are encouraging, although the heterogeneity of the rat head and the experimental com-

plexity on a live animal bring more difficulties. Using a baseline image calibration technique, the functional changes during the hypoxia were well traced by NIR images and show a good correlation to the blood-oxygen-level-independent signal.

With this versatile dual-modality system, we will put more effort not only into understanding the use of high-resolution MRI structural information in diffuse image reconstruction but also in applying it to the biological study of brain hypoxia and ischemia as well as pathologies such as stroke, tumors, and asphyxia, which all induce changes in oxygenation and hemodynamics.

References

1. F. F. Jobsis, "Non-invasive, infra-red monitoring of cerebral and myochardial oxygen sufficiency and circulatory parameters," Science **198,** 1264–1267 (1977).

2. B. Chance, S. Nioka, J. Kent, K. McCully, M. Fountain, R. Greenfield, and G. Holtom, "Time-resolved spectroscopy of hemoglobin and myoglobin in resting and ischemic muscle," Anal. Biochem. **174,** 698–707 (1988).

3. O. Hazeki and M. Tamura, "Quantitative analysis of hemoglobin oxygenation state of rat brain *in situ* by near-infrared spectrophotometry," J. Appl. Physiol. **64,** 796–802 (1988).

4. M. Haida and B. Chance, "A method to estimate the ratio of absorption coefficients of two wavelengths using phase modulated near infrared light spectroscopy," Adv. Exp. Med. Biol. **345,** 829–835 (1994).

5. S. J. Matcher and C. E. Cooper, "Absolute quantification of deoxyhaemoglobin concentration in tissue near infrared spectroscopy," Phys. Med. Biol. **39,** 1295–1312 (1994).

6. N. Ramanujam, M. F. Mitchell, A. Mahadevan, S. Thomsen, A. Malpica, T. Wright, N. Atkinson, and R. Richards-Kortum, "Spectroscopic diagnosis of cervical intraepithelial neoplasia (CIN) *in vivo* using laser-induced fluorescence spectra at multiple excitation wavelengths," Lasers Surg. Med. **19,** 63–74 (1996).

7. B. J. Tromberg, O. Coquoz, J. B. Fishkin, T. Pham, E. R. Anderson, J. Butler, M. Cahn, J. D. Gross, V. Venugopalan, and D. Pham, "Non-invasive measurements of breast tissue optical properties using frequency-domain photon migration," Philos. Trans. R. Soc. London Ser. B **352,** 661–668 (1997).

8. S. Srinivasan, B. W. Pogue, S. Jiang, H. Dehghani, C. Kogel, S. Soho, J. J. Gibson, T. D. Tosteson, S. P. Poplack, and K. D. Paulsen, "Interpreting hemoglobin and water concentration, oxygen saturation, and scattering measured *in vivo* by near-infrared breast tomography," Proc. Natl. Acad. Sci. USA **100,** 12349–12354 (2003).

9. S. J. Matcher, M. Cope, and D. T. Delpy, "Use of the water absorption spectrum to quantify tissue chromophore concentration changes in near-infrared spectroscopy," Phys. Med. Biol. **39,** 177–196 (1994).

10. S. J. Matcher, M. Cope, and D. T. Delpy, "*In vivo* measurements of the wavelength dependence of tissue-scattering coefficients between 760 and 900 nm measured with time-resolved spectroscopy," Appl. Opt. **36,** 386–396 (1997).

11. E. L. Hull, M. G. Nichols, and T. H. Foster, "Quantitative broadband near-infrared spectroscopy of tissue-simulating phantoms containing erythrocytes," Phys. Med. Biol. **43,** 3381–3404 (1998).

12. S. R. Arridge and M. Schweiger, "Image reconstruction in optical tomography," Philos. Trans. R. Soc. London Ser. B **352,** 717–726 (1997).

13. M. Schweiger and S. R. Arridge, "Comparison of two- and three-dimensional reconstruction methods in optical tomography," Appl. Opt. **37,** 7419–7428 (1998).

14. H. Dehghani, B. W. Pogue, J. Shudong, B. Brooksby, and K. D. Paulsen, "Three-dimensional optical tomography: resolution in small-object imaging," Appl. Opt. **42,** 3117–3128 (2003).

15. B. W. Pogue, S. P. Poplack, T. O. McBride, W. A. Wells, K. S. Osterman, U. L. Osterberg, and K. D. Paulsen, "Quantitative hemoglobin tomography with diffuse near-infrared spectroscopy: pilot results in the breast," Radiology **218,** 261–266 (2001).

16. A. Gibson, R. M. Yusof, H. Dehghani, J. Riley, N. Everdell, R. Richards, J. C. Hebden, M. Schweiger, S. R. Arridge, and D. T. Delpy, "Optical tomography of a realistic neonatal head phantom," Appl. Opt. **42,** 3109–3116 (2003).

17. H. Xu, B. W. Pogue, H. Dehghani, R. Springett, K. D. Paulsen, and J. F. Dunn, "Feasibility of NIR tomographic reconstruction with multispectral continuous wave data by mapping into frequency domain data," in *Optical Tomography and Spectroscopy of Tissue V*, B. Chance, R. R. Alfano, B. J. Tromberg, M. Tamura, and E. M. Sevick-Muraca, eds., Proc. SPIE **4955,** 103–114 (2003).

18. H. Xu, B. W. Pogue, H. Dehghani, and K. D. Paulsen, "Absorption and scattering imaging of tissue with steady-state second-differential spectral-analysis tomography," Opt. Lett. **29,** 2043–2045 (2004).

19. M. Schweiger and S. R. Arridge, "Optical tomographic reconstruction in a complex head model using *a priori* region boundary information," Phys. Med. Biol. **44,** 2703–2721 (1999).

20. B. A. Brooksby, H. Dehghani, B. W. Pogue, and K. D. Paulsen, "Near-infrared (NIR) tomography breast image reconstruction with *a priori* structural information from MRI: algorithm development for reconstructing heterogeneities," IEEE J. Sel. Top. Quantum Electron. **9,** 199–209 (2003).

21. V. Ntziachristos, X. H. Ma, and B. Chance, "Time-correlated single photon counting imager for simultaneous magnetic resonance and near-infrared mammography," Rev. Sci. Instrum. **69,** 4221–4233 (1998).

22. Q. Zhu, N. Chen, and S. H. Kurtzman, "Imaging tumor angiogenesis by use of combined near-infrared diffusive light and ultrasound," Opt. Lett. **28,** 337–339 (2003).

23. A. Li, E. L. Miller, M. E. Kilmer, T. J. Brukilacchio, T. Chaves, J. Stott, Q. Zhang, T. Wu, M. Chorlton, R. H. Moore, D. B. Kopans, and D. A. Boas, "Tomographic optical breast imaging guided by three-dimensional mammography," Appl. Opt. **42,** 5181–5190 (2003).

24. B. W. Pogue and K. D. Paulsen, "High resolution near infrared tomographic imaging simulations of rat cranium using *a priori* MRI structural information," Opt. Lett. **23,** 1716–1718 (1998).

25. H. Xu, H. Dehghani, B. W. Pogue, R. Springett, K. D. Paulsen, and J. F. Dunn, "Near-infrared imaging in the small animal brain: optimization of fiber positions," J. Biomed. Opt. **8,** 102–110 (2003).

26. T. O. McBride, B. W. Pogue, S. Jiang, U. L. Osterberg, and K. D. Paulsen, "Development and calibration of a parallel modulated near-infrared tomography system for hemoglobin imaging *in vivo*," Rev. Sci. Instrum. **72,** 1817–1824 (2001).

27. B. L. Horecker, "The absorption spectra of hemoglobin and its derivatives in the visible and near infrared regions," J. Biol. Chem. **148,** 173–183 (1943).

28. V. S. Hollis, "Non-invasive monitoring of brain tissue temperature by near-infrared spectroscopy," Ph.D. thesis (University College London, 2002).

29. R. F. Reinoso, B. A. Telfer, and M. Rowland, "Tissue water content in rats measured by desiccation," J. Pharmacol. Toxicol. Methods **38,** 87–92 (1997).

30. M. Schweiger, S. R. Arridge, M. Hiraoka, and D. T. Delpy, "The finite element method for the propagation of light in scattering media: boundary and source conditions," Med. Phys. **22,** 1779–1792 (1995).

31. H. B. Jiang, K. D. Paulsen, U. L. Osterberg, B. W. Pogue, and M. S. Patterson, "Simultaneous reconstruction of optical-absorption and scattering maps in turbid media from near-infrared frequency-domain data," Opt. Lett. **20,** 2128–2130 (1995).

32. D. W. Marquardt, "An algorithm for least-squares estimation of nonlinear parameters," J. Soc. Indust. Appl. Math. **11,** 431–441 (1963).

33. B. W. Pogue, T. O. McBride, J. Prewitt, U. L. Osterberg, and K. D. Paulsen, "Spatially variant regularization improves diffuse optical tomography," Appl. Opt. **38,** 2950–2961 (1999).

34. K. D. Paulsen and H. Jiang, "Spatially varying optical property reconstruction using a finite element diffusion equation approximation," Med. Phys. **22,** 691–701 (1995).

35. H. Dehghani, M. M. Doyley, B. W. Pogue, S. Jiang, J. Geng, and K. D. Paulsen, "Breast deformation modelling for image reconstruction in near infrared optical tomography," Phys. Med. Biol. **49,** 1131–1145 (2004).

36. D. M. Hueber, M. A. Franceschini, H. Y. Ma, Q. Zhang, J. R. Ballesteros, S. Fantini, D. Wallace, V. Ntziachristos, and B. Chance, "Non-invasive and quantitative near-infrared haemoglobin spectrometry in the piglet brain during hypoxic stress, using a frequency-domain multidistance instrument," Phys. Med. Biol. **46,** 41–62 (2001).

37. C. Julien-Dolbec, I. Tropres, O. Montigon, H. Reutenauer, A. Ziegler, M. Decorps, and J. F. Payen, "Regional response of cerebral blood volume to graded hypoxic hypoxia in rat brain," Br. J. Anaesth. **89,** 287–293 (2002).

38. S. Punwani, C. E. Cooper, M. Clemence, J. Penrice, P. Amess, J. Thornton, and R. J. Ordidge, "Correlation between absolute deoxyhaemoglobin [dHb] measured by near infrared spectroscopy (NIRS) and absolute R2′ as determined by magnetic resonance imaging (MRI)," Adv. Exp. Med. Biol. **413,** 129–137 (1997).

39. Y. Chen, D. R. Tailor, X. Intes, and B. Chance, "Correlation between near-infrared spectroscopy and magnetic resonance imaging of rat brain oxygenation modulation," Phys. Med. Biol. **48,** 417–427 (2003).

40. I. Kida, T. Yamamoto, and M. Tamura, "Interpretation of BOLD MRI signals in rat brain using simultaneously measured near-infrared spectrophotometric information," NMR Biomed. **9,** 333–338 (1996).

41. B. A. Brooksby, S. Jiang, G. Ehret, H. Dehghani, B. W. Pogue, and K. D. Paulsen, "Development of a system for simultaneous MRI and near-infrared diffuse tomography to diagnose breast cancer," in *Biomedical Topical Meetings* (CD-ROM) (Optical Society of America, Washington, D.C., 2004).

42. B. A. Brooksby, S. Jiang, H. Dehghani, B. W. Pogue, K. D. Paulsen, C. Kogel, M. Doyley, J. B. Weaver, and S. P. Poplack, "Magnetic resonance-guided near-infrared tomography of the breast," Rev. Sci. Instrum. **75,** 5262–5270 (2004).